

UC Davis

UC Davis Previously Published Works

Title

PICASSO: a universal brain phantom for positron emission tomography based on the activity painting technique

Permalink

<https://escholarship.org/uc/item/1384485m>

Journal

Physics in Medicine and Biology, 69(21)

ISSN

0031-9155

Authors

Shanina, Ekaterina
Spencer, Benjamin A
Li, Tiantian
[et al.](#)

Publication Date

2024-11-07

DOI

10.1088/1361-6560/ad84b5

Copyright Information

This work is made available under the terms of a Creative Commons Attribution License, available at <https://creativecommons.org/licenses/by/4.0/>

Peer reviewed

PICASSO: A universal brain phantom for positron emission tomography based on the activity painting technique

Ekaterina Shanina^{1*}, Benjamin A. Spencer², Tiantian Li^{1,3}, Bangyan Huang¹, Jinyi Qi¹ and Simon R. Cherry^{1,2}

¹ Department of Biomedical Engineering, University of California, Davis, Davis, CA, USA

² Department of Radiology, University of California, Davis, Sacramento, CA, USA

³ United Imaging Healthcare, Houston, TX, USA

* Author to whom any correspondence should be addressed.

Email: eshanina@ucdavis.edu

Keywords: positron emission tomography (PET), phantoms, brain imaging

Abstract.

Objective. This study presents a universal phantom for positron emission tomography (PET) that allows arbitrary static and dynamic activity distributions of various complexities to be generated using a single PET acquisition.

Approach. We collected a high-statistics dataset (with a total of 22.4×10^9 prompt coincidences and an event density of 2.75×10^6 events/mm³) by raster-scanning a single plane with a ²²Na point source mounted on a robotic arm in the field-of-view of the uEXPLORER PET/CT scanner. The source position was determined from the reconstructed dynamic frames. Uniquely, true coincidences were separated from scattered and random events based on the distance between their line-of-response and the known source location. Finally, we randomly sampled the dataset to generate the desired activity distributions modeling several different phantoms.

Main results. Overall, the target and the reconstructed phantom images had good agreement. The analysis of a simple geometric distribution showed high quantitative accuracy of the phantom, with mean error of $< -3.0\%$ relative to the ground truth for activity concentrations ranging from 5.3 to 47.7 kBq/ml. The model of a high-resolution ¹⁸F-fluorodeoxyglucose distribution in the brain illustrates the usefulness of the technique in simulating realistic static neuroimaging studies. A dynamic ¹⁸F-florbetaben study was modeled based on a time-activity curve of a human study and a segmented brain phantom with no coincidences repeating between frames. For all time points, the mean voxel-wise errors ranged from -4.4% to -0.7% in grey matter and from -3.9% to $+2.8\%$ in white matter.

Significance. The proposed phantom technique is highly flexible and allows modeling of static and dynamic brain PET studies with high quantitative accuracy. It overcomes several key limitations of the existing phantoms and has many promising applications for the purposes of image reconstruction, data correction methods, and system performance evaluation, particularly for new high-performance dedicated brain PET scanners.

1. Introduction

Positron emission tomography (PET) provides excellent opportunities to study the brain, including its neurochemistry, pathology, and drug interactions [1]. While it is certainly possible to image the brain with conventional clinical whole-body PET scanners, such systems are not optimized for neuroimaging, and their limited spatial resolution restricts the achievable image quality. Recently, there has been a lot of interest in developing high-resolution PET scanners dedicated to brain imaging [2]. Now in addition to the HRRT (CTI/Siemens) [3] which has been the state-of-the-art brain imaging system for over two decades, there are several released and upcoming systems, such as the NeuroEXPLORER PET/CT scanner (United Imaging Healthcare) [4], the SAVANT standalone PET system [5], the Human Dynamic NeuroChemical Connectome (HDNCC) PET insert for 7-tesla magnetic resonance imaging (MRI) scanners [6], NeuroLF (Positron AG) [7], Pharos (Brightonix Imaging Inc.) [8], and others. To evaluate and optimize the performance of these new brain scanners, we need appropriate imaging phantoms.

There are two general classes of PET phantoms: digital and physical. Digital phantoms rely on simulation models rather than data from an actual scanner. Their main advantage is that they require no physical production and handling (i.e., filling and scanning), which makes them easy to modify and use for modeling of arbitrary radiotracer distributions. However, the usefulness of digital phantoms depends on how accurately the simulation reproduces the system, certain aspects of which are difficult to model accurately. These include dead time, variable spatial resolution across the field of view (FOV), and precise details on how the scanner electronics and software select valid events, position them, and implement energy and timing windows.

Physical phantoms are real objects that can range from relatively simple (e.g., point and line sources) to quite complex phantoms designed to model parts of the human body. While simple sources are generally used to measure system performance (e.g., image quality, sensitivity, spatial resolution) [9], anthropomorphic phantoms may be better suited to estimate scanner performance in actual human imaging scenarios. Some of the most commonly used human brain phantoms are the 3D Hoffman phantom [10] and the Iida phantom [11]. Although these and other similar phantoms are widely used, they have a number of inherent limitations. Despite being only a few hundred microns in thickness, the physical walls that separate activity levels in these phantoms significantly complicate the quantification analysis, as one must specifically model the cold wall and account for partial volume effects when evaluating fine structures. Furthermore, most physical phantoms reflect the static regional distribution of a particular radiotracer and usually do not allow for an easy introduction of small changes in the phantom (e.g., insertion of a lesion, change of contrast) within a single study. Liquid-filled phantoms with complex internal structure are difficult to fill without air bubbles which interfere with imaging. Finally, physical phantoms are typically proprietary and rather expensive.

More importantly, these state-of-the-art brain phantoms may not be appropriate for the new high-performance scanners. It has been shown that the composite slice structure of the Hoffman phantom becomes resolvable on high-resolution systems [12], which means it is no longer possible to rely on the partial volume effect to simulate the grey-to-white matter activity ratio. Measurements of the Iida phantom show the smallest cortical thicknesses of approximately 2.5-3.0 mm, so the physical dimensions of the phantom are larger than the measured or projected spatial resolution of the new dedicated-brain systems. However, further reduction of the fillable phantom feature size will likely further complicate the filling process. Thus, there is clearly a need for novel PET phantoms, especially for neuroimaging applications.

Recently, a new and rather unconventional PET phantom design was proposed [13,14], which overcomes several key limitations of both physical and digital phantoms. The technique involves "painting" the desired distribution with a radioactive point source in the FOV of a PET scanner. The source is stepped through a given trajectory with a high-precision programmable system; contrast is generated by varying the amount of time the source stays at different spatial locations. The technique is highly reproducible and allows one to model any activity distribution within any region of the body without the need for cumbersome preparation involving liquid radioactive sources. At the same time, structures can be defined at an arbitrarily fine scale in the absence of physical walls separating different activity levels. The phantom inherently contains scanner parameters that are difficult to model computationally or theoretically.

The original approach requires a new acquisition for each desired activity distribution. In this work, we propose a more efficient method that allows modeling of any activity pattern using data from a single acquisition. This can be done by collecting one spatially uniform, very high-statistics dataset and sampling it to select the needed number of events in every voxel. The PICASSO (**p**ainting with radio**i**sotopes for **c**oincidence **a**cquisition and **s**ampling to **s**hape an **o**bject) approach can be used to efficiently generate a variety of phantoms that model arbitrary activity distributions in the brain or other body regions with various feature sizes, radiotracers, and injected activity and noise levels. It is relatively straightforward to change contrast or modify the activity distribution. If the number of collected events is sufficiently large, we can model dynamic scans by generating multiple dynamic frames without reusing data, so that each frame consists of completely independent data, thus avoiding any artificial correlation between frames. Another unique feature of this phantom design is the ability to discriminate true coincidences from random and scattered events based on the distance between their line-of-response (LOR) and the known point source location. If the scatter fraction in the coincidence event pool is low, we can generate datasets with different randoms fractions, which would aid in more accurate modeling of different activity levels and in evaluating the accuracy of randoms correction methods.

The applications of the PICASSO phantom are numerous: it can be used to (1) test reconstruction algorithms and data correction methods and assess quantitative recovery in every voxel, (2) evaluate spatial resolution at different locations within the FOV, (3) build an accurate system model for image reconstruction, (4) generate a diverse dataset for training deep learning algorithms, and (5) produce physiologically meaningful dynamic scans, which may be of particular use to inform the development and testing of kinetic modeling techniques, especially with regards to their sensitivity to different noise levels and initialization conditions, as well as optimization of framing protocols for dynamic studies.

Here we present the methodology of the PICASSO phantom and its application in modeling static and dynamic neurological imaging studies. In this initial work, we collected a planar dataset approximately equal in size to a cross-section of an adult human brain and sampled it to generate simple geometric and complex anthropomorphic activity distributions. We also investigate the quantitative accuracy of the proposed technique and illustrate how the randoms fraction in the phantom datasets can be varied. In the discussion section, we describe the extension of our methodology to three dimensions and propose approaches to modeling scatter and attenuation.

2. Materials and methods

The novelty of the PICASSO phantom approach, outlined in Figure 1, is that virtually any desired PET activity pattern can be generated from a single dataset. It involves a one-time acquisition of a uniform, very high-statistics data pool with a sealed point source moving in the FOV of a PET scanner and subsequent sampling of this data pool to produce the phantom data files.

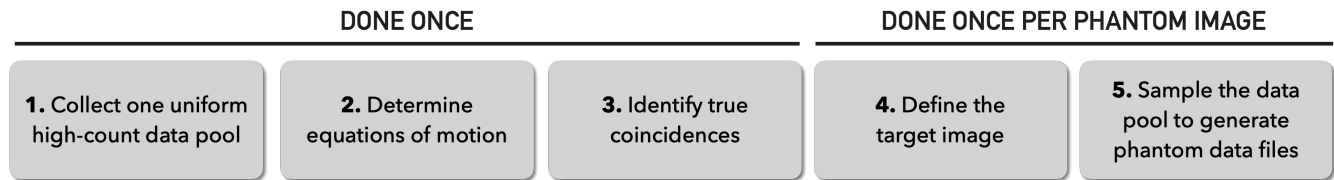


Figure 1: Summary of the data processing steps.

2.1. Data acquisition

To collect the spatially uniform high-statistics coincidence event pool, we affixed a high-precision robotic arm (Denso Robotics, VP series) to the patient bed of the uEXPLORER total-body PET/CT scanner (United Imaging Healthcare) and used it to translate a point source in the FOV of the scanner as it continuously acquired data (Figure 2a). Although not a dedicated brain scanner, the uEXPLORER is a good development platform because it has high spatial resolution (<3 mm) for a whole-body scanner [15], comparable to the HRRT. In addition, this choice of scanner allowed us to take advantage of our in-house reconstruction framework, which is important for initial implementation and validation of the phantom methodology.

Source: In our experiments, we used a ^{22}Na source. Although this radionuclide is not used for *in vivo* imaging, it is a good surrogate for two of the most common PET isotopes – ^{18}F and ^{11}C – in terms of the average positron range. The longer half-life of 2.6 years makes ^{22}Na particularly convenient in this application, as the data can be acquired without significant decay of activity throughout the acquisition. At the same time, using a carefully calibrated sealed source simplifies the experiment setup.

The phantom event density (number of decays per unit volume) must be sufficiently high to support modeling of meaningful brain images. In a typical ^{18}F -fluorodeoxyglucose (FDG) scan, grey matter activity is expected to be approximately 25–50 kBq/ml [4,16]. Thus, to reproduce a single 30-minute scan, the collected decay density must be on the order of at least 10^5 events/ mm^3 .

The decay density is a function of the source activity and speed with which it is translated by the robot. A high-activity source allows collecting the desired count level faster. However, activity is proportional to the source size, which must be sufficiently small to avoid degrading the spatial resolution of the phantom images. In our study, we used a cylindrical source with 1-mm diameter and 1-mm height; at the time of acquisition, the source activity was 27.5 MBq (0.742 mCi). According to our calculations, a 1-mm diameter point source would degrade the image resolution by less than 2.5% beyond the spatial resolution of the uEXPLORER (reported to be 2.4–4.7 mm [15]). Thus, the phantom image resolution is dominated by the resolution of the scanner, and the contribution of the finite source size is relatively small. Importantly, the same source would cause an up to 3% degradation in image resolution if used with HRRT (with the spatial resolution of 2.3–5.7 mm [3]), and up to 7% degradation with the NeuroEXPLORER (with the spatial resolution of 1.43–3.05 mm [4]), so the source size needs to be selected with the imaging system in mind. The source was enclosed in cylindrical plastic casing (25.2-mm diameter, 53.6-mm height) to achieve similar scattering in all directions and attached to the robotic arm via a 30-cm stainless steel optical post to reduce attenuation caused by the body of the robot.

Motion parameters: The source raster-scanned the phantom image space moving at a constant speed along the axial direction (Figure 2b). In this study, the source traversed a single 220×180 mm² coronal plane in air in the center of the FOV. The plane orientation was chosen arbitrarily. A speed of 10 mm/s was selected to maximize the resulting count density while maintaining a reasonable acquisition time.

To obtain a spatially uniform activity distribution, the step size between neighboring lines had to be sufficiently small such that individual lines could not be resolved on the reconstructed image. The step size of 1 mm was selected experimentally. Notably, it is less than half the spatial resolution of the scanner (estimated to be 2.4–3.2 mm for iterative reconstruction [15]) and matches the size of the point source.

With the parameters selected for the experiment, we acquired 22.4 billion prompt and 5.8 billion delayed coincidences over the course of approximately 66 minutes. The phantom had a decay density of 2.75×10^6 events/mm³, which is sufficient to model several independent acquisitions or multiple frames of the same dynamic study with no data reuse between frames. Note that although this is a planar dataset, we chose to use a volumetric rather than areal decay density for easy scalability of the experiment to three dimensions.

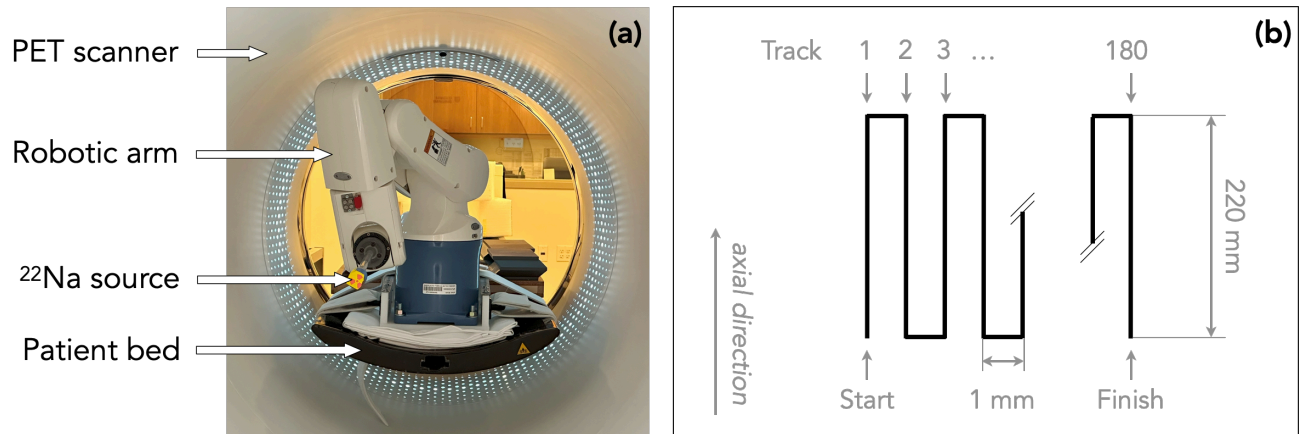


Figure 2: (a) Experimental setup. The robotic arm mounted at the superior end of the patient bed moves a ²²Na point source in the FOV of the uEXPLORER total-body PET/CT scanner. (b) Schematic source trajectory.

2.2. Equations of motion

To determine the equations of motion of the source in the scanner coordinate system, we divided the total-volume listmode file into 1-second frames (with about 5.6×10^6 prompt and 4.2×10^6 true coincidences in each frame) and reconstructed them using the ordered subset expectation maximization (OSEM) algorithm (1 iteration, 1 subset, no attenuation correction, no point spread function (PSF) modeling, 0.95-mm isotropic voxels). The reconstruction parameters were chosen in order to achieve minimal convergence to allow for more voxels to be used for the estimation of source position, calculated as the centroid of the reconstructed activity distribution in each frame (Figure 3a). For every track, defined as a single axial line traveled by the source, we obtained the equations of motion by performing linear fitting of source coordinates in time (Figure 3b) and used these equations to define the voxels in the phantom image space (Figure 3c). The voxel size was chosen to be $1 \times 1 \times 1$ mm³, less than $\frac{1}{2}$ of the spatial resolution of the scanner. Thus, the phantom image matrix was $220 \times 180 \times 1$ voxels.

2.3. True coincidence identification

For each prompt event, the line of response (LOR) was defined as the line connecting the centers of crystals where annihilation gamma interaction was detected. The source-to-LOR distance is the perpendicular length between the point source location and the LOR.

Based on the experimental distributions of distances for prompt and delayed events, a threshold of 24 mm was selected, and all events with source-to-LOR distances exceeding the threshold were excluded. The randoms fraction in the dataset before and after the source-to-LOR distance filtering were 26% and 0.16%, respectively, as estimated using the delayed-window method. In addition to removing random and scattered coincidences, this procedure also removed the undesired coincidences formed by the 1275-keV prompt gamma with a 511-keV annihilation photon from the same decay of a ^{22}Na atom.

In the case of the simple geometric phantom (described in section 2.4), a more rigorous source-to-LOR distance threshold of 5 mm was additionally used to further reduce the amount of random and scattered coincidences and evaluate the quantitative accuracy of the approach.

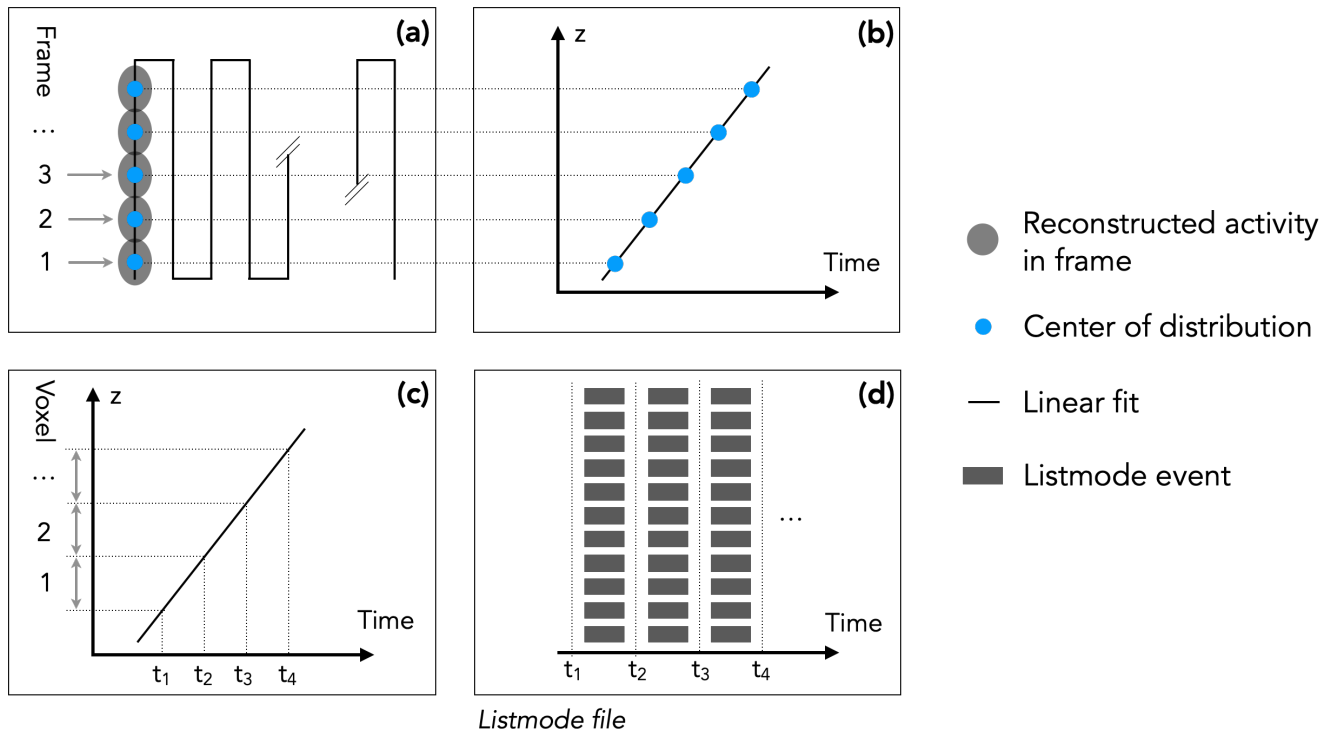


Figure 3: Schematic illustration of the method used to obtain the equations of motion. (a) Data was divided into short frames, then each frame was reconstructed, and source position was calculated as the center of mass of the reconstructed activity distribution. (b) Linear fitting was performed to define equations of motion. (c) Voxel start and end times were determined from the equations of motion. (d) For each voxel, the desired number of events can be randomly selected based on the desired activity concentration in the target image using the voxel start and end times.

2.4. Phantoms

To demonstrate the flexibility in creating different phantom shapes, we used several target 2D patterns. Each pattern was specified as a 220×180 matrix of activity concentration values. Given that the spatial resolution of the scanner is limited, there is no obvious advantage for the target pattern to have a substantially higher spatial resolution.

A simple geometric distribution was modeled after the transverse slice of the NEMA NU 2-2018 [9] image quality (IQ) phantom centered on the hot spheres. First, a 1:1 scale image was

constructed using the phantom dimensions specified in the standard, except the diameter of all hot spheres was set to 37 mm. Then the final pattern was obtained by scaling the 1:1 image down by a factor of 2/3 for the phantom to fit in the 220×180 matrix; the resulting hot sphere diameters were 24 mm. The background activity concentration was set to 5.3 kBq/ml, and concentrations in the spheres were 1.5, 3, 4.5, 6, 7.5, and 9 times that of the background; the central region (equivalent to the lung insert in the NEMA IQ phantom) had an activity concentration of zero. The modeled scan duration was chosen to be 30 minutes.

A single slice of the high-resolution Belzunce brain phantom [17] representing the ^{18}F -FDG uptake in a healthy brain was used to illustrate the use of the PICASSO phantom technique in modeling complex anthropomorphic activity distributions. The original phantom slice was resized to fit the phantom matrix and normalized; the highest voxel activity concentration value was set to 50 kBq/ml. The scan length was set to 30 minutes.

Finally, we used a single slice of the 3D Hoffman brain phantom [18] as a simplified human brain model with segmented grey and white matter regions to reproduce a dynamic study. The activity values for grey and white matter were obtained from the time-activity curves (TACs) of ^{18}F -florbetaben in a healthy subject approximated from the experimental TACs reported in [19]. The standardized uptake values (SUVs) were converted to activity concentrations by assuming a patient mass of 70 kg and injected activity of 300 MBq, and activity-time products were extracted at six timepoints by integrating the TAC over the frame duration. The modeled frames were: 60-90 s, 5-6 min, 20-23 min, 34-39 min, 50-55 min, and 75-80 min. For simplicity, the activity concentration within the same tissue type was assumed to be uniform within each frame. No adjustments of SUVs due to decay were made.

2.5. Random sampling

Finally, to produce the phantom data files based on the target activity concentration map, we randomly sampled the phantom data pool using the voxel start and end times determined from the equations of motion (Figure 3d). For each voxel, we calculated the ratio between the target decay density (activity-time product) and the true decay density, defined by the point source activity, its speed, and spatial sampling rate. Subsequently, each prompt event with source-to-LOR distance below 24 mm was selected with a probability equal to that ratio. In the case of a dynamic study, coincidence sampling was performed for all frames in parallel, such that each coincidence could be selected for no more than one frame.

Overall, the analysis did not require significant computational resources. The unsampled phantom dataset occupied 267 GB. The calculation of the equations of motion, coincidence filtering for a given source-to-LOR distance threshold, and listmode sampling were carried out using the code package developed for this project running on a Lenovo ThinkPad P14s laptop with Intel Core i7 2.8-GHz processor and 16-GB RAM; the code did not employ parallel computing. Depending on the total activity in the phantom, the sampling took approximately 30 minutes for a one-frame static study and 90 minutes for a six-frame dynamic study.

2.6. Image reconstruction and analysis

All subsampled phantom datasets were reconstructed using a desired static reconstruction protocol (OSEM algorithm, 4 iterations, 13 subsets, no attenuation correction, no PSF modeling, 1-mm isotropic voxels, no smoothing filters), including the dynamic frames which were reconstructed individually.

To assess quantitative accuracy of the phantom, we performed a region-of-interest (ROI) analysis of the simple geometric distribution. A circular ROI was drawn concentric to each of the six hot circular regions and one cold circular region; the ROI radius was $2/3$ of the radius of the corresponding circular region to reduce the spill-in and partial volume effect at the region boundaries. Additionally, twelve circular ROIs were drawn in the background region; the background ROIs had the same size as the hot spheres. The percent error was calculated for every ROI voxel in reference to the known target activity concentration. In addition, the mean and standard deviation of the activity concentration was calculated across each ROI in the hot spheres and in the cold region, as well as across twelve background ROIs.

For the Hoffman phantom, ROIs were placed on the grey and white matter regions with a 3-mm offset from the region's boundary, again to reduce the partial volume effect. The voxel-wise percent error as well as the ROI statistics (mean and standard deviation) were calculated using these ROIs for each frame in the dynamic study model.

3. Results

3.1. Phantom dataset characteristics

The experimental source trajectory reconstructed from the frame-wise centroid calculation is shown in Figure 4a. Due to a slight misalignment between the internal axes of the robot and those of the scanner during setup, the plane does not coincide exactly with the intended coronal plane; on average, the tracks made an angle of $2.02^\circ \pm 0.02^\circ$ with the coronal plane and an angle of $0.07^\circ \pm 0.04^\circ$ with the sagittal plane. This misalignment does not affect the phantom accuracy as the source position is known in three dimensions at all timepoints from the reconstructed image frames, and each voxel value can be assessed using its absolute coordinates.

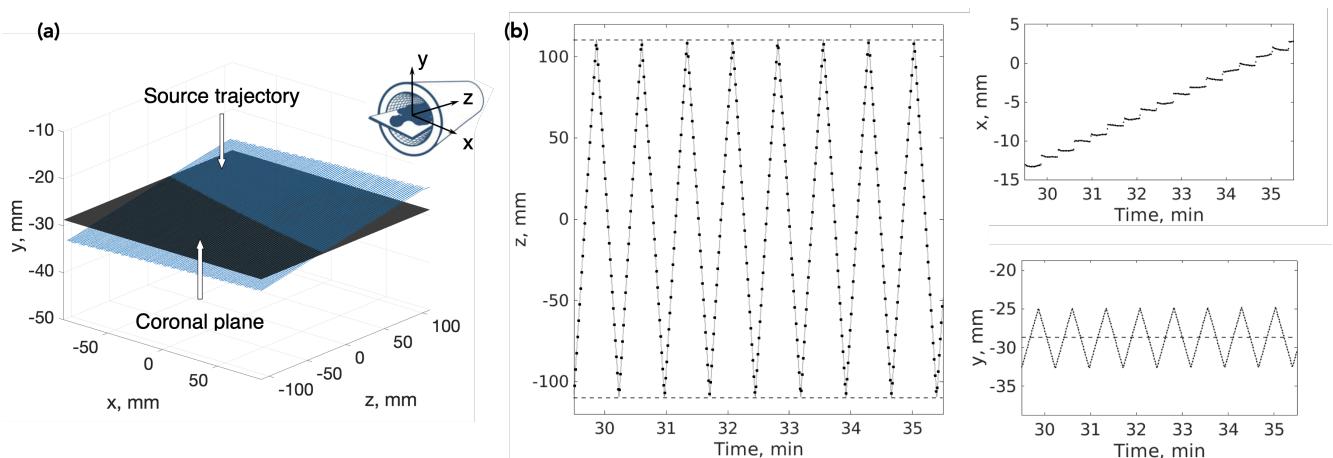


Figure 4: (a) Reconstructed source trajectory (blue) relative to the (shifted) coronal plane of the scanner (black). (b) Plotted equations of motion of the source. Points with the same y values lie on the same coronal plane, those with the same x values - on the same sagittal plane, and those with the same z values - on the same transverse plane.

Figure 4b shows the source coordinates as a function of time. The source traveled back and forth along the z -axis sweeping the plane from one side to the other. Each line on the $z(t)$ plot corresponds to a single 220-mm axial track. The value of x increases in a series of 180 steps, each of which corresponds to the transaxial coordinate of a single track. Finally, $y(t)$ deviates from the $y = 0$ line (corresponding to a single coronal plane) due to the misalignment mentioned earlier.

The experimental source speed was estimated as a slope of the linear fit for each track on the $z(t)$ plot. The calculated value of 9.988 ± 0.001 mm/s is rather uniform and closely matches the speed of 10 mm/s set on the robot controller.

3.2. Modeling of static studies

There is good agreement between the target patterns and the sampled and reconstructed phantom images for the simple geometric activity distribution and the high-resolution ^{18}F -FDG distribution shown in Figure 5. The major differences between the reconstructed phantom and the ground truth images are at activity boundaries and are caused by differences in spatial resolution, which is lower for the reconstructed images due to the finite spatial resolution of the scanner.

To assess the quantitative accuracy of the PICASSO phantom, two profiles were drawn through the images of the IQ-like geometric pattern: a vertical profile through the center and a circular profile centered at the cold inner region. The phantom activity concentration values were calculated from the reconstructed image matrix at the absolute phantom voxel positions using bilinear interpolation. Figure 6 shows very close match between the ground truth and the phantom profiles. The edge smoothing observed at the region boundaries is caused by the partial volume effect.

The results of the ROI analysis (Figure 7) further corroborate the high accuracy of the phantom image. The mean errors in the hot spheres ranged from -1.3% to -3.0% relative to the ground truth without any obvious dependence on the activity within the spheres. The mean background error was -0.9% , and the activity concentration in the cold region of the phantom was 6.4 Bq/ml – almost three orders of magnitude below the background level. For all ROIs, the phantom appears to underestimate the target concentration, which is likely due to a small amount of scatter present in the dataset. When a more rigorous source-to-LOR distance threshold of 5 mm was used, the phantom accuracy slightly improved, with mean errors in the hot spheres ranging from -0.7% to $+1.3\%$, and a mean background error of -1.0% .

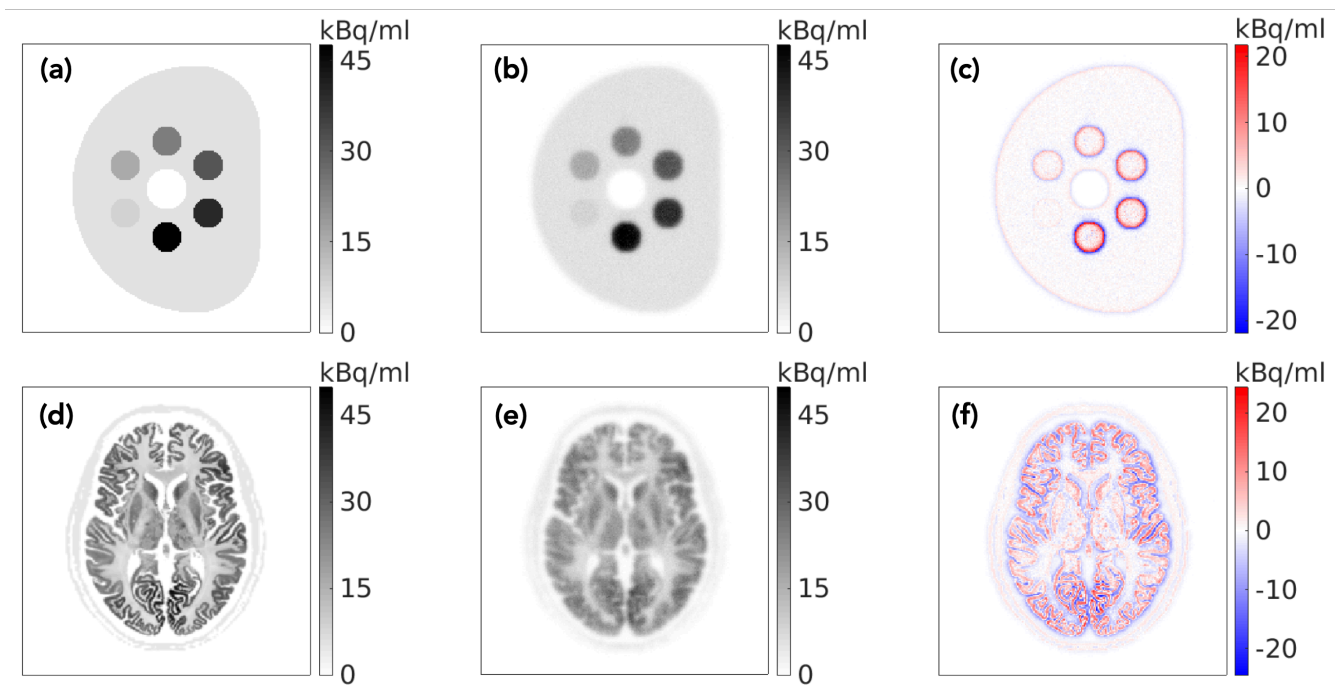


Figure 5: (a) Target and (b) reconstructed phantom images of the simple geometric distribution. (d) A single slice of the high-resolution ^{18}F -FDG phantom and (e) reconstructed phantom image. (c) and (f) show the difference between the target and phantom images. Because of the slight misalignment of the phantom plane relative to the scanner axes, the reconstructed images are displayed as projections along the y-axis.

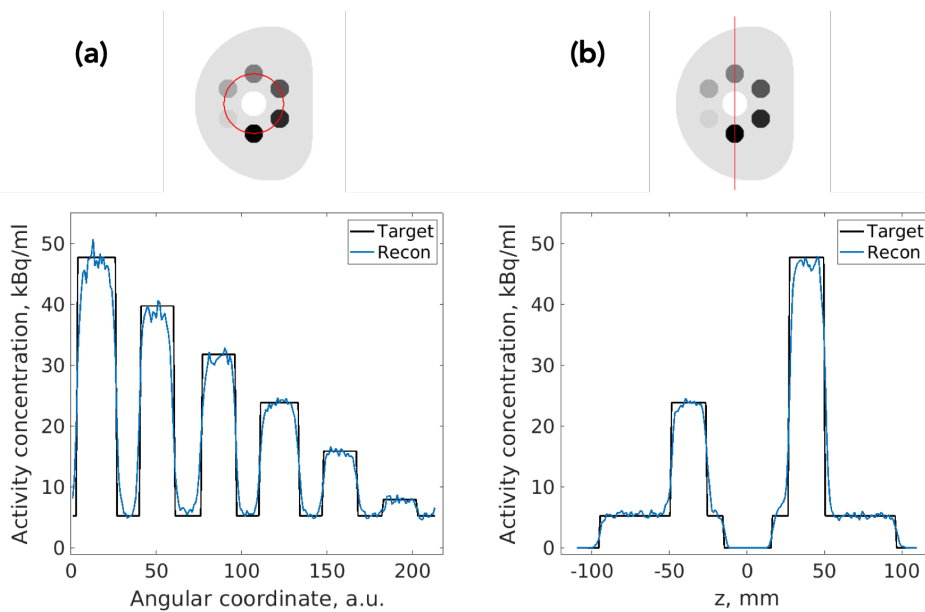


Figure 6: Line profiles through the simple geometric phantom. (a) Circular profile centered at the cold region. (b) Vertical profile through the center of the phantom.

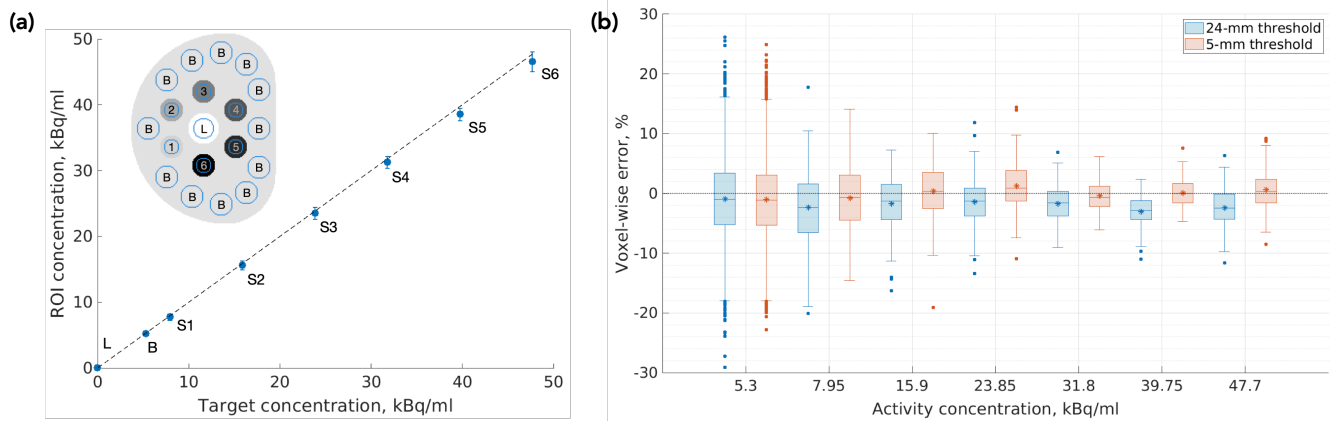


Figure 7: (a) Mean (\pm std) experimental activity concentrations calculated from ROIs against the ground truth activity concentration for the simple geometric distribution. Six ROIs were placed on the hot circular regions (1-6), one ROI – on the central cold region (L), and twelve ROIs – on the background region (B). (b) Percent error calculated for each ROI voxel in reference to the ground truth activity concentration for two source-to-LOR distance thresholds. (Note: source-to-LOR distance threshold affects the randoms and scatter fraction of the phantom data pool.) The statistics shown are the median (horizontal bar), lower and upper quartiles (shaded region), minimum and maximum values that are not outliers (whiskers), and outliers (filled points); the mean error is depicted with an asterisk (*).

3.3. Modeling of dynamic studies

Figure 8a shows the TACs used to extract the target SUVs (continuous lines); the reconstructed phantom frames are shown in Figure 8b. Scatter points overlaid on the TACs are the mean experimental SUVs calculated from the grey and white matter ROIs placed on phantom images as shown in Figure 8d. For all frames, the mean phantom SUVs are within one standard deviation of the ground truth values. The statistics of the voxel-wise percent error analysis are summarized in Figure 8c. Notably, mean grey matter errors ranged from -4.4% to -0.7% , and mean white matter errors were between -3.9% and $+2.8\%$. The 60-90 sec frame spanned the greatest range of values due to the low statistics in the frame caused by the short frame duration and low activity values, especially in the white matter region.

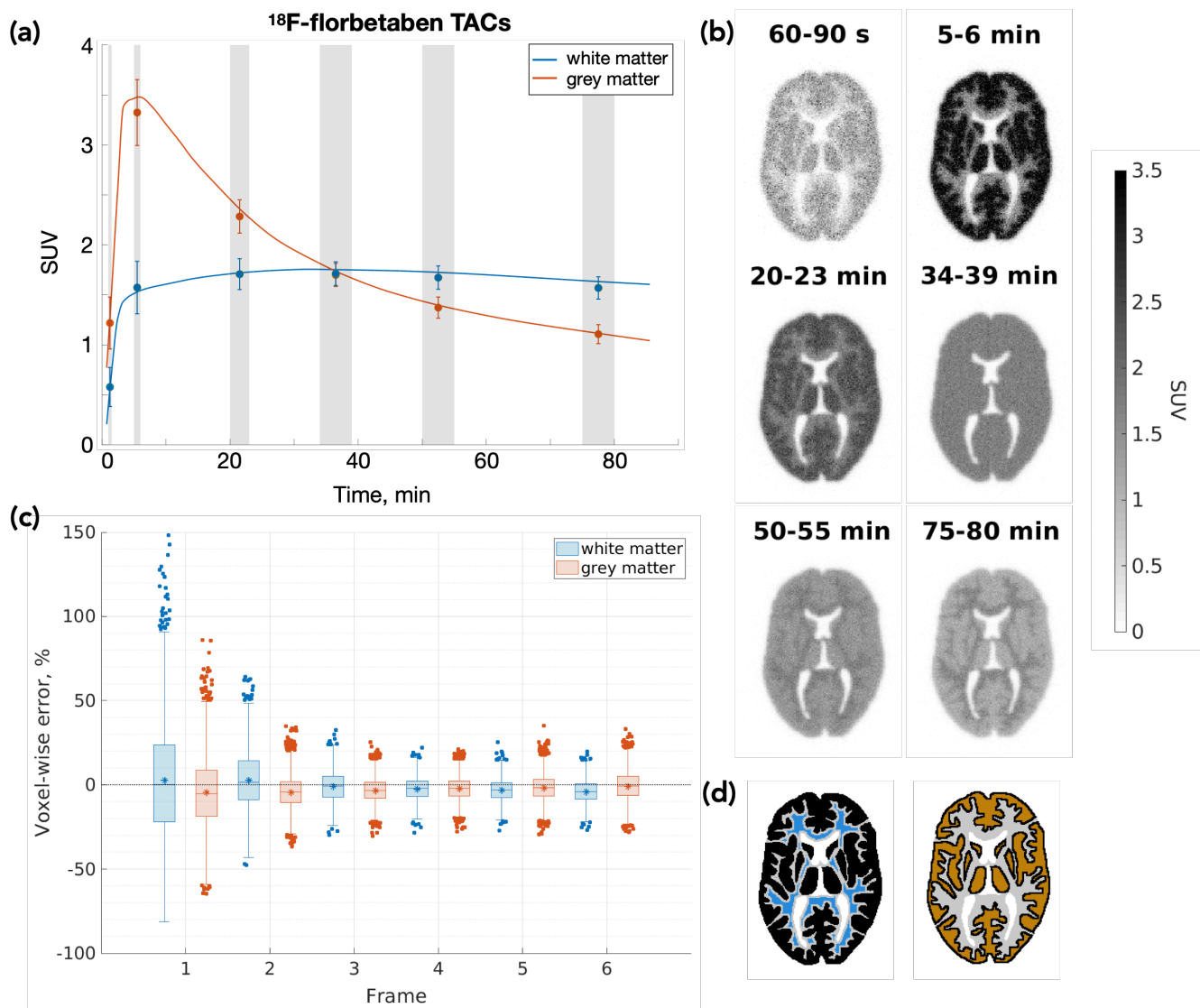


Figure 8: Dynamic study model. (a) *Continuous lines*: TACs of the ^{18}F -florbetaben concentration in healthy grey and white matter used to define SUVs in the phantom regions; *scatter points*: mean (\pm std) experimental SUV measured from the phantom images. Shaded regions represent frames. (b) Sampled and reconstructed phantom frames at six different time points. (c) Percent error calculated for each ROI voxel in reference to the ground truth activity concentration for grey and white matter. The mean error is depicted with an asterisk (*). (d) White and grey matter ROIs placed on each phantom frame.

4. Discussion

Previously, the technique of “painting” the desired activity pattern with a point source in the FOV of the scanner was used to produce one activity distribution per acquisition [13,14]. In this work, we developed the PICASSO approach, the goal of which is to acquire a single uniform high-statistics dataset and sample it to obtain a multitude of desired activity distributions, modeling different radiotracers, geometries, and activity levels. We demonstrated the use of our phantom in modeling static and dynamic studies with no data overlap between frames.

Another key benefit of the PICASSO phantom is the ability to effectively remove the erroneous events formed by an annihilation photon and a high-energy prompt gamma emitted in

coincidence with the positron (e.g., the 1275-keV prompt gamma of ^{22}Na). If the gamma scatters in the detector and deposits an energy that is within the scanner energy window, the coincidence event formed by the prompt gamma and the annihilation photon would result in source mispositioning. Our analysis of the ^{22}Na data indicates that there is a significant number of such events even with a relatively narrow energy window of 430–645 keV: about 50% of prompt coincidences had source-to-LOR distances above 24 mm, while the randoms fraction estimated by the delayed window method was only 26%. Thus, it appears that approximately 24% of prompt events involved prompt gamma or were scattered. Given that the source moved in air, we expect the amount of scattering to be relatively low, which is also supported by the slight underestimation of the target activity concentration by the phantom seen in Figure 7. The conclusion that the observed phenomenon can be mainly attributed to the prompt gamma is also supported by the experimental data involving an ^{18}F -FDG point source, where 28% of prompt coincidences had source-to-LOR distance above the threshold of 24 mm, and the delayed-window-based randoms fraction was 23%. Thus, the ability to selectively remove events formed by prompt emissions is highly valuable when using one radionuclide to model another.

It is important to note the limitations of the current experimental setup and how they can be addressed to further extend the applicability and scientific value of the proposed PICASSO phantom technique. First, moving the source in air in the absence of scattering media does not allow modeling of realistic attenuation and scatter of annihilation photons within the body. In a future study, we are planning to address this by introducing a volume of tissue-like scattering media (e.g., water) around the source. A homogeneous medium would likely be a reasonable way of modeling tissue scatter and attenuation in the brain. In the case of body regions with more heterogeneous tissue makeup (e.g., torso), attenuation can be easily modeled during post-processing by discarding events based on attenuation probability; however, accurate modeling of scatter is more complex and would require careful consideration.

Furthermore, the phantom may not accurately represent random coincidences and dead time. If the scatter fraction is low, the randoms fraction within sampled data can be varied, as each event can be labeled as a random or true coincidence based on the distance between its LOR and the source. However, the situation is more complicated if the data contains a significant amount of scatter (e.g., when scattering media is present), as the method cannot differentiate random events from scattered coincidences.

Finally, the physical properties of ^{22}Na , the radionuclide of choice in this study, are well-matched to ^{18}F and ^{11}C in terms of positron range. However, if the radiotracer of interest uses a radionuclide with significantly different physical properties, it might be necessary to acquire a new phantom data pool using a radionuclide with better-matched positron range. If the decay scheme of this radionuclide contains prompt emissions, they can be removed using the source-to-LOR distance analysis, as discussed earlier.

Overall, the planar dataset we used in this first study clearly demonstrated the promise of the PICASSO phantom. Work is underway to extend our methodology to three dimensions. We are aiming to collect data over a volume approximately equal in size to an adult human brain and apply the methodology we have developed to characterize and process this dataset. Such 3D dataset would allow us to model realistic activity distributions in the entire human brain and further explore the clinical applications of this phantom. The main challenge is to develop efficient methods to handle and process the extremely large dataset (estimated to be as much as 10 TB).

Of course, the methodology described here is not limited to a specific scanner. In future, we will also focus on acquiring a phantom dataset on the NeuroEXPLORER to take advantage of the high spatial resolution of this dedicated brain scanner for modeling of yet more detailed activity distributions in the human brain (for example, cortical ribbon structures and small nuclei that have been resolved with the NeuroEXPLORER [4,19]). An important advantage of this technique is that voxel size, and hence the spatial resolution of the phantom can be chosen depending on the scanner or the desired application, although the point source size and the spatial sampling frequency (i.e., separation distance between neighboring tracks) will need to be re-evaluated.

Given that acquisition and initial processing of a large phantom dataset could be expensive in terms of time and resources needed to obtain and program the source translation system and characterize the source motion, it is our intent to share the acquired dataset with the research community directly, once we successfully extend our technique to 3D and when the community has agreed upon a common vendor-agnostic format for sharing listmode data [21,22]. Since, in theory, we only need one dataset for each scanner type, it is possible to create a collection of such datasets acquired on different scanners and use them for scanner comparison.

The proposed phantom technique is incredibly versatile and can be used for applications well beyond neuroimaging, including, but not limited to other organ imaging, small-animal imaging, and likely even whole-body imaging, although precise long-range source movement and long acquisition times may become challenging. One solution would be to augment physical phantom or human data with the PICASSO phantom data (e.g., by adding features or lesions), which would aid in reducing acquisition time and modeling realistic scatter and attenuation properties of the target object.

5. Conclusions

In this study, we developed a method of acquiring a single uniform high-statistics dataset and sampling it to efficiently generate a variety of activity distributions – the PICASSO phantom. We showed how it can be used to model realistic static and dynamic neuroimaging studies and demonstrated very good quantitative accuracy in phantom images.

The proposed approach overcomes several key limitations of both physical and digital phantoms, as it allows modeling activity distributions of various complexities and arbitrarily fine features without the need for cumbersome preparation and analysis methods, and the data intrinsically contains some of the scanner parameters that are difficult to model analytically. We believe the PICASSO phantom has many promising applications for the purposes of image reconstruction, data correction methods, and system performance evaluation.

6. Acknowledgements

This work was supported by NIH grant U01 EB029811. The authors would like to thank Drs. Junwei Du, Justin Ellin, Reimund Bayerlein, and Negar Omidvari for their scientific input and insightful discussions during this project. We are also grateful to the anonymous reviewers for their comments and suggestions, which helped us in improving the quality of this manuscript.

UC Davis has a research agreement and a sales-based revenue-sharing agreement with United Imaging Healthcare. No other potential conflict of interest relevant to this article was reported.

7. References

- [1] J. M. Hooker and R. E. Carson, "Human positron emission tomography neuroimaging," *Annu. Rev. Biomed. Eng.*, vol. 21, no. 1, pp. 551–581, 2019, doi: 10.1146/annurev-bioeng-062117-121056.
- [2] C. Catana, "Development of dedicated brain PET imaging devices: Recent advances and future perspectives," *J. Nucl. Med.*, vol. 60, no. 8, pp. 1044–1052, Aug. 2019, doi: 10.2967/jnumed.118.217901.
- [3] H. W. A. M. de Jong, F. H. P. van Velden, R. W. Kloet, F. L. Buijs, R. Boellaard, and A. A. Lammertsma, "Performance evaluation of the ECAT HRRT: An LSO-LYSO double layer high resolution, high sensitivity scanner," *Phys. Med. Biol.*, vol. 52, no. 5, p. 1505, Feb. 2007, doi: 10.1088/0031-9155/52/5/019.
- [4] H. Li *et al.*, "Performance Characteristics of the NeuroEXPLORER, a Next-Generation Human Brain PET/CT Imager," *J. Nucl. Med.*, Jun. 2024, doi: 10.2967/jnumed.124.267767.
- [5] R. Lecomte *et al.*, "Scanner Approaching in Vivo Autoradiographic Neuro Tomography (SAVANT): Progress towards μ L resolution for imaging the human brain," *J. Nucl. Med.*, vol. 63, no. supplement 2, pp. 2436–2436, Jun. 2022.
- [6] M. Scipioni *et al.*, "Design and Development of the Human Dynamic NeuroChemical Connectome Scanner," in *2023 IEEE Nuclear Science Symposium, Medical Imaging Conference and International Symposium on Room-Temperature Semiconductor Detectors (NSS MIC RTSD)*, Nov. 2023, pp. 1–2. doi: 10.1109/NSSMICRTSD49126.2023.10337891.
- [7] M. Jehl *et al.*, "Attenuation correction using template PET registration for Brain PET: A proof-of-concept study," *J. Imaging*, vol. 9, no. 1, Art. no. 1, Jan. 2023, doi: 10.3390/jimaging9010002.
- [8] G. B. Ko *et al.*, "Initial assessment of the physical and in-vivo performance of 3-module-ring Pharos PET system," *J. Nucl. Med.*, vol. 64, no. supplement 1, pp. P912–P912, Jun. 2023.
- [9] *NEMA standards publication NU 2-2018: performance measurements of positron emission tomographs (PET)*, NU 2-2018, 2018.
- [10] E. J. Hoffman, P. D. Cutler, W. M. Digby, and J. C. Mazziotta, "3-D phantom to simulate cerebral blood flow and metabolic images for PET," *IEEE Trans. Nucl. Sci.*, vol. 37, no. 2, pp. 616–620, Apr. 1990, doi: 10.1109/23.106686.
- [11] H. Iida *et al.*, "Three-dimensional brain phantom containing bone and grey matter structures with a realistic head contour," *Ann. Nucl. Med.*, vol. 27, no. 1, pp. 25–36, Jan. 2013, doi: 10.1007/s12149-012-0655-7.
- [12] D. Morimoto-Ishikawa *et al.*, "Evaluation of the performance of a high-resolution time-of-flight PET system dedicated to the head and breast according to NEMA NU 2-2012 standard," *EJNMMI Phys.*, vol. 9, no. 1, p. 88, Dec. 2022, doi: 10.1186/s40658-022-00518-3.
- [13] A. Forgacs *et al.*, "Activity painting: PET images of freely defined activity distributions applying a novel phantom technique," *PLOS ONE*, vol. 14, no. 1, p. e0207658, Jan. 2019, doi: 10.1371/journal.pone.0207658.

- [14] A. Paramithas, "Evaluation of a robotic painting phantom to optimise the quantification accuracy of tau PET/CT images," Doctor of Clinical Science, University of Manchester, 2022.
- [15] B. A. Spencer *et al.*, "Performance evaluation of the uEXPLORER total-body PET/CT scanner based on NEMA NU 2-2018 with additional tests to characterize PET scanners with a long axial field of view," *J. Nucl. Med.*, vol. 62, no. 6, pp. 861–870, Jun. 2021, doi: 10.2967/jnumed.120.250597.
- [16] M. Villien *et al.*, "Dynamic functional imaging of brain glucose utilization using fPET-FDG," *NeuroImage*, vol. 100, pp. 192–199, Oct. 2014, doi: 10.1016/j.neuroimage.2014.06.025.
- [17] M. A. Belzunce and A. J. Reader, "Technical note: Ultra high-resolution radiotracer-specific digital pet brain phantoms based on the BigBrain atlas," *Med. Phys.*, vol. 47, no. 8, pp. 3356–3362, 2020, doi: 10.1002/mp.14218.
- [18] R. L. Harrison, B. F. Elston, D. W. Byrd, A. M. Alessio, K. R. Swanson, and P. E. Kinahan, "Technical note: A digital reference object representing Hoffman's 3D brain phantom for PET scanner simulations," *Med. Phys.*, vol. 47, no. 3, pp. 1174–1180, 2020, doi: 10.1002/mp.14012.
- [19] G. A. Becker *et al.*, "PET Quantification of 18F-Florbetaben Binding to β -Amyloid Deposits in Human Brains," *J. Nucl. Med.*, vol. 54, no. 5, pp. 723–731, May 2013, doi: 10.2967/jnumed.112.107185.
- [20] R. Carson *et al.*, "Exceptional Brain PET Images from the NeuroEXPLORER: Scans with Targeted Radiopharmaceuticals and Comparison to HRRT," *J. Nucl. Med.*, vol. 65, no. supplement 2, pp. 241473–241473, Jun. 2024.
- [21] K. Thielemans *et al.*, "The PET Raw Data Standardization Initiative," *J. Nucl. Med.*, vol. 64, no. supplement 1, pp. P687–P687, Jun. 2023.
- [22] N. Karakatsanis *et al.*, "Usability of PETSIRD, the PET Raw Data open format of the Emission Tomography Standardization Initiative (ETSI): Results from ETSI's first hackathon," *J. Nucl. Med.*, vol. 65, no. supplement 2, pp. 241285–241285, Jun. 2024.